

## SPITZER IRAC PHOTOMETRY FOR TIME SERIES IN CROWDED FIELDS

S. CALCHI NOVATI<sup>1,2,3,10</sup>, A. GOULD<sup>4</sup>, J. C. YEE<sup>5,11</sup>, C. BEICHMAN<sup>1</sup>, G. BRYDEN<sup>6</sup>, S. CAREY<sup>7</sup>, M. FAUSNAUGH<sup>4</sup>, B. S. GAUDI<sup>4</sup>,  
C. B. HENDERSON<sup>6,4,12</sup>, R. W. POGGE<sup>4</sup>, Y. SHVARTZVALD<sup>6,12</sup>, B. WIBKING<sup>4</sup>, W. ZHU<sup>4</sup>

(SPITZER TEAM),

AND

A. UDALSKI<sup>8</sup>, R. POLESKI<sup>4</sup>, M. PAWLAK<sup>8</sup>, M. K. SZYMAŃSKI<sup>8</sup>, J. SKOWRON<sup>8</sup>, P. MRÓZ<sup>8</sup>, S. KOZŁOWSKI<sup>8</sup>, Ł. WYRZYKOWSKI<sup>8</sup>,  
P. PIETRUKOWICZ<sup>8</sup>, G. PIETRZYŃSKI<sup>8</sup>, I. SOSZYŃSKI<sup>8</sup>, AND K. ULACZYK<sup>9</sup>

(OGLE GROUP)

<sup>1</sup> NASA Exoplanet Science Institute, MS 100-22, California Institute of Technology, Pasadena, CA 91125, USA

<sup>2</sup> Dipartimento di Fisica “E. R. Caianiello,” Università di Salerno, Via Giovanni Paolo II, I-84084 Fisciano (SA), Italy

<sup>3</sup> Istituto Internazionale per gli Alti Studi Scientifici (IIASS), Via G. Pellegrino 19, I-84019 Vietri Sul Mare (SA), Italy

<sup>4</sup> Department of Astronomy, Ohio State University, 140 W. 18th Ave., Columbus, OH 43210, USA

<sup>5</sup> Harvard-Smithsonian Center for Astrophysics, 60 Garden St., Cambridge, MA 02138, USA

<sup>6</sup> Jet Propulsion Laboratory, California Institute of Technology, 4800 Oak Grove Drive, Pasadena, CA 91109, USA

<sup>7</sup> *Spitzer*, Science Center, MS 220-6, California Institute of Technology, Pasadena, CA, USA

<sup>8</sup> Warsaw University Observatory, Al. Ujazdowskie 4, 00-478 Warszawa, Poland

<sup>9</sup> Department of Physics, University of Warwick, Gibbet Hill Road, Coventry, CV4 7AL, UK

Received 2015 August 31; accepted 2015 October 13; published 2015 November 19

## ABSTRACT

We develop a new photometry algorithm that is optimized for the Infrared Array Camera (IRAC) *Spitzer* time series in crowded fields and that is particularly adapted to faint or heavily blended targets. We apply this to the 170 targets from the 2015 *Spitzer* microlensing campaign and present the results of three variants of this algorithm in an online catalog. We present detailed accounts of the application of this algorithm to two difficult cases, one very faint and the other very crowded. Several of *Spitzer*’s instrumental characteristics that drive the specific features of this algorithm are shared by *Kepler* and *WFIRST*, implying that these features may prove to be a useful starting point for algorithms designed for microlensing campaigns by these other missions.

**Key words:** gravitational lensing: micro – techniques: photometric

**Supporting material:** figure set

## 1. INTRODUCTION

The Infrared Array Camera (IRAC) on the *Spitzer* observatory has been employed in a vast array of scientific investigations, including some that were not imagined at the time it was launched in 2003, much less when it was conceived in the 1980s. Perhaps the most famous of these is the measurement of differential exoplanet transit depth as a function of wavelength, which requires exquisite photometric precision in order to probe the exo-atmospheres (Charbonneau et al. 2005; Deming et al. 2005). These and other applications have stimulated the development of new photometric techniques and pipelines.

In the last two years, *Spitzer* has taken on a completely new role as a “microlens parallax satellite” (Refsdal 1966). Although this application was suggested prior to launch (Gould 1999), and even carried out for one event (OGLE-2005-SMC-001, Dong et al. 2007), the photometric advances required to meet this role were not even basically understood until data were collected from the 2014 “pilot program”: 100 hours of Director’s Discretionary Time that were granted to assess the feasibility of *Spitzer* microlens parallaxes. These data revealed that while standard (*Spitzer* or other) photometric packages returned reasonably good photometry for most bright events (Calchi Novati et al. 2015; Udalski et al. 2015b; Yee et al.

2015b; Zhu et al. 2015b), these packages usually failed, often catastrophically, for faint events.

After 832 hr were awarded for the 2015 season (i.e., the majority of the 38 days for which *Spitzer* can observe Galactic-bulge microlensing fields during microlensing season), Yee et al. (2015a) developed detailed protocols to optimize efficiency to achieve the program’s primary aim of measuring the “Galactic distribution of planets.” Of course, one of the key parameters in these protocols was an estimate of the IRAC 3.6  $\mu\text{m}$  threshold at which one could expect reliable *Spitzer* photometry. Yee et al. (2015a) reviewed the results from various photometric packages as applied to the 2014 campaign to establish a threshold assuming no further improvements, which they parameterized by a 3.6  $\mu\text{m}$  flux indicator<sup>13</sup>  $L_{\text{eff}} = 15.5$ . They also analyzed the reasons for the shortcomings of existing packages when applied to this data set and reported in outline the ongoing work (now presented in the current paper) to resolve these shortcomings.

One of the key points made by Yee et al. (2015a) was that the selection of targets had to balance two critical indicators, encapsulated in a “quality factor,” which sums over all observed events,  $i$ :

$$Q = \sum_i S_i P_i \quad (1)$$

<sup>10</sup> Sagan Visiting Fellow.

<sup>11</sup> Sagan Fellow.

<sup>12</sup> NASA Postdoctoral Program Fellow.

<sup>13</sup>  $L_{\text{eff}} = I - 0.93 A_I - 1.3 + 0.5\Theta(I - A_I - 17.2)$ , where  $\Theta$  is a step function and  $A_I$  is the extinction.

where  $S_i$  is the planet sensitivity and  $P_i$  is the probability that the observations would return a reliable microlens parallax (which of course requires reliable *Spitzer* photometry). This implied that events with exceptional sensitivity (large  $S_i$ ) should be observed despite great risk (low  $P_i$ ) that they would be too faint by the time *Spitzer* observed them, which could be from 3 to 10 days after they were recognized as sensitive to planets based on their ground-based light curves (Figure 1 of Udalski et al. 2015b).

The main class of such ultrasensitive events is high-magnification events (Griest & Safizadeh 1998; Gould et al. 2010), which in most cases cannot be predicted until a few days before peak. Hence, in most cases, by the time that *Spitzer* observed such a high-magnification event, it would already be well past peak and therefore very faint. Acting on the basis of Equation (1), however, the *Spitzer* microlens team typically attempted to observe such high-magnification events even when the expected  $3.6\ \mu\text{m}$  flux was well below the threshold identified by Yee et al. (2015a). In fact, seven high-magnification events (with peak magnifications  $A > 100$ ) were observed, which greatly exceeded expectations. This also greatly increased the stakes of improving the photometric performance at faint flux levels.

More generally, *Spitzer* microlens targets can be subject to extreme crowding, which can critically impact the photometry of these sources even when they are relatively bright. This can in turn adversely affect a range of applications, from measuring microlens parallaxes to using the *Spitzer* light curves themselves to detect planets (Gould & Horne 2013).

The protocol for the target selection for the 2015 *Spitzer* campaign is described in detail in Yee et al. (2015a). A key point is that *Spitzer* targets can be chosen “objectively” or “subjectively,” according to whether they fulfill, or not, a set of specified criteria. This is relevant first to establish the cadence of the observations and second to frame the analysis of the planet sensitivity.

In Section 2, we review the challenges to obtaining excellent time series photometry in crowded fields with *Spitzer* using existing packages, and we outline our algorithm for meeting these challenges. In Section 3, we discuss present applications of this algorithm to two examples of the difficult conditions encountered while pursuing the above scientific objectives. In Section 4, we describe an online catalog of photometry from our pipeline for all of the 170 events observed by *Spitzer* in the 2015 campaign. As we note there, it may often be possible to improve on this pipeline photometry for individual events of special scientific interest. The first author should therefore be contacted regarding applications of this photometry. Finally, in Section 5, we discuss some future implications of this work.

## 2. CHALLENGES TO CROWDED-FIELD PHOTOMETRY WITH *Spitzer*

Broadly, there are two classes of routines applicable to time series photometry in crowded fields using electronic detectors: multiobject point-spread function (PSF) photometry (MOPSF) and difference imaging analysis (DIA).

MOPSF (e.g., DoPhot, Schechter et al. 1993) was originally designed to disentangle stars in single-epoch images of crowded fields, such as globular clusters. Once an ensemble of point sources is identified, they are fit either individually or in groups to an ensemble of overlapping PSFs. In principle, this

routine can be applied to a time series by simply repeating the operation on many frames and cross-identifying point sources. However, if the cadence is high (so that the stars can be approximated as not moving between epochs), then the stability of the results can be improved by enforcing fixed positions on the stars. This is particularly relevant for applications such as microlensing in which one star may substantially change brightness while the others remain roughly constant. In that case, if the star positions are not held fixed, they may drift under the influence of changing flux ratios of overlapping PSFs, including unresolved (i.e., unmodeled) blends.

DIA (e.g., Alard & Lupton 1998) works by a completely different principle. No attempt is made to identify stars. Rather, an essentially noise-free template is created by stacking good-seeing images. Each image in the series is then aligned photometrically and geometrically with the template, and the template is convolved with a kernel to make its PSF similar to that of the current image. Then the current image is subtracted from the convolved template. Stars that have varied then appear as PSF bumps or divots. Usually these are isolated and so can easily be centroided and then multiplied by the PSF to yield a photometric measurement. DIA has proved so far superior to MOPSF that the latter is rarely used for time series photometry in crowded fields. At the same time, however, it is obviously useless for photometry of constant stars since these simply disappear from the difference images.

Neither of these techniques is suitable for the analysis of faint variable targets in crowded *Spitzer* images.

For the *Spitzer* microlensing campaign, we use channel 1 (at  $3.6\ \mu\text{m}$ ) of the IRAC camera (Fazio et al. 2004) with mean pixel scale  $1''.221$  and mean FWHM  $1''.66$ , with the image quality being limited primarily by the telescope optics. Given our goal of performing point-source photometry in a crowded field, it is important to note that the PSF is undersampled and that there is a significant variation in sensitivity within pixels (i.e., with the “pixel phase”; Ingalls et al. 2012). To address these issues, the *Spitzer* Science Center developed an approach based on point response functions (PRFs) specific to IRAC (a technique previously developed for the WFPC2 and NICMOS on the *Hubble Space Telescope*; Lauer 1999; Anderson & King 2000). These are meant to combine information about the PSF, the detector sampling, and the intrapixel sensitivity variation.<sup>14</sup> The *Spitzer* Science Center has also developed a specific package, MOPEX (Makovoz & Marleau 2005), to deal with the various aspects of the *Spitzer* instrument image analysis, and specifically for the photometry of point sources for IRAC.

We pause to note why the standard MOPSF and DIA packages are bound to fail, at least in the more difficult situations of low signal-to-noise ratio (S/N) or crowding. DIA does not work because it implicitly assumes a uniform pixel response, a condition that is not met for IRAC. MOPSF also does not work, but not for such a fundamental reason. The underlying logic of standard MOPSF is actually very similar to MOPEX, but it is not built to deal with the PRFs. In this sense MOPEX can be considered a specialized variant of MOPSF.

For *Spitzer* microlensing observations, each “epoch” of a given target is composed of six 30 s exposures, each dithered by a few arcseconds. The *Spitzer* pipeline (in particular, MOPEX) also provides, in addition to these single frames, a

<sup>14</sup> <http://irsa.ipac.caltech.edu/data/SPITZER/docs/dataanalysis/tools/mopex/mopexusersguide/home/>

mosaic of the dithers of a given epoch. We remark that a PRF analysis only makes sense when applied to the single-frame images. This information is blurred away in the mosaic frames, which come, on the other hand, with a higher S/N and look similar to optical CCD images. Standard photometry techniques, such as aperture photometry, MOPSF, and DIA, can be applied to these images, and for bright or isolated stars the results can be passable to good. However, for faint stars in more crowded situations the results can be poor to catastrophic.

Point-source photometry requires first a point-source extraction and second a flux determination. In our analysis we take advantage of two facts, which then require us to update and refine the MOPEX approach accordingly. First, we possess quite accurate prior knowledge of essentially all significant  $3.6\,\mu\text{m}$  sources on the frame. Second, we are dealing with a time series of images for which, as a working hypothesis, *one can assume that only the microlensed source varies*, with all other neighboring stars assumed constant, including those that are heavily blended with the microlensed source. (In principle, it is possible that a neighboring star can be a variable. However, it is straightforward to identify such stars from the residuals and to grant them an extra flux parameter for each epoch instead of imposing a single constant-flux parameter.)

As foreshadowed, for point-source photometry, MOPEX works according to essentially the same principles as DoPhot, but with the specialized feature of employing PRFs. In essence, the photometry procedure is a fit based on a  $\chi^2$  minimization where the signal, over the area of interest (a few pixels around each target), is modeled as a background term plus a linear sum of the PRFs of the different sources contributing to each pixel. There are therefore three free parameters for each source: an amplitude term, which multiplies the corresponding PRF, and a pair of coordinates specifying the source centroid. As a technical point, we note that the PRF is sampled at  $5 \times 5 = 25$  pixel phase positions, i.e., five steps across the pixel in each direction. This is the basis for interpolating the PRF at each specific pixel phase.<sup>15</sup> MOPEX can perform this fitting scheme working on single frames individually or on multiple frames simultaneously, including frames belonging to different epochs. From our standpoint, the drawback of MOPEX is its rigidity: it does not allow us to take advantage of the two aforementioned facts specific to our problem. In particular, the only choice permitted by MOPEX is whether to leave the background term as a free parameter. The flux and positions of all the stars involved must always be fitted, which in our case means for each individual epoch (since the microlensed source flux changes with epoch). For this reason, the PRF-fitting MOPEX indeed works well with our data for sufficiently isolated or bright sources. However, especially for faint stars, it sometimes cannot locate the star at all, or if it can, it incorrectly locates the centroid because of confusion of blended objects and so applies the wrong PRF. Or, what is potentially worse, as the microlensed source gets brighter and fainter, MOPEX shifts its estimate of the centroid, leading to systematic errors that vary with changing brightness. For the 2014 campaign, MOPEX worked reasonably well for about half of the sample. It worked poorly for about one-quarter of

the sample and failed catastrophically for the remaining quarter. MOPEX fared much worse on the 2015 sample because the microlensed sources were overall substantially fainter.

From an algorithmic standpoint, the path to resolving the difficulties faced by MOPEX is straightforward: apply the same improvements made to DoPhot and other MOPSF packages when they graduated from single-epoch to time series applications. First, one should hold the brightness of all stars fixed from epoch to epoch (after establishing that they are not in fact variable). Second, one should (usually) hold fixed the angular offsets between all stars from one epoch to the next.

Implementation of the first (photometric) constraint is straightforward. If there are  $N$  epochs,  $n$  nonvarying stars in the neighborhood of the lens, and  $m \geq 1$  varying stars (including the lens), then there are a total of  $n + mN + 1$  photometric parameters (including one for the background).

However, it is not obvious how to implement the second (astrometric) constraint, or even whether to do so. At the outset, prior to and independent from the photometric analysis, we build a relative astrometric solution to link the Optical Gravitational Lens Experiment (OGLE) (or in some cases, MOA) catalog coordinates<sup>16</sup> to the *Spitzer* pixel coordinates, and this for each one of the  $6N$  IRAC frames. In one case (Method 2, below) we additionally need a relative astrometric solution between an arbitrarily chosen IRAC “reference” frame and the other IRAC frames.

The great majority of  $3.6\,\mu\text{m}$  sources in most microlensing fields are known with good astrometric precision from OGLE catalogs, which have much better resolution than *Spitzer*. A first approach is simply to adopt these positions. In this case, we determine the positions of each star in each *Spitzer* frame, including the microlensing source, from a local ensemble of reference-star triangles.

Second, one can use the OGLE positions as inputs to derive the IRAC positions from a simultaneous fit to all frames. Then there are  $(6qN + 2(n + m))$  parameters, that is, some number  $q \geq 6$  frame-transformation parameters for each of the  $6N$  images, which are applied prior to the analysis of each image, and the two-dimensional offsets of each star from a fiducial origin, which is held fixed for all  $6N$  images. More specifically, to carry out the relative astrometry we make use of the IRAF package geomap with a polynomial nonlinear transformation of order 5–8. The typical astrometric uncertainty that we achieve is about 0.1 pixel.

Finally, one can use the OGLE positions as inputs, but derive star positions on each frame separately. From the standpoint of astrometry, this is similar to what MOPEX does on a single frame (although it still differs from MOPEX in that it imposes a photometric constraint). In this case, there are  $6N \times 2(n + m)$  astrometric parameters.

In brief, the methods are as follows:

Method 1: Externally determined PRF centroid

Method 2: Single PRF centroid from simultaneous fit to all epochs

Method 3: Individually fitted PRF centroid for each frame

<sup>15</sup> In the current analysis we make use of the publicly available cold-mission PRFs. These are, however, expected to have changed since 2009 when *Spitzer* entered its warm-mission operational phase (Storrie-Lombardi & Dodd 2010). We have tested our algorithm using a preliminary version of the warm-mission PRFs (J. Ingalls 2015, private communication), and we do not find substantial differences in the output photometry.

<sup>16</sup> All *Spitzer* targets are selected from ongoing microlensing events that have been publicly alerted by either the Optical Gravitational Lens Experiment (OGLE) or Microlensing Observations in Astrophysics (MOA) collaborations. Each OGLE alert is linked to a detailed photometric and astrometric catalog of neighboring stars.



We find that, in the majority of cases, Method 2 works best, but Methods 1 and 3 do sometimes work better.

Specifically, if the microlensed source is extremely faint, there is almost no information in any of the images about the location of this source, so the OGLE information of this source position (which is very precise because it comes from astrometry of the difference image between when it is magnified and at baseline) is far superior to what can be obtained by fitting the IRAC images. Hence, Method 1 works best for these sources.

If the microlensed source has considerable signal even in just a subset of images, then PRF fits to its position are usually superior to those derived from the transformation from the OGLE frame. This is an empirical fact. Its cause is not completely understood but is most likely due to a combination of errors in the frame transformations and the different distributions of I-band and  $3.6\ \mu\text{m}$  light in these crowded fields. Hence, either Method 2 or Method 3 is better.

If the microlensed source is sometimes relatively bright and sometimes quite faint, then Method 2 works well but Method 3 fails because the lens position is “lost” on the fainter images. By the nature of the *Spitzer* microlensing campaign, this is true in the majority of cases. However, if the microlensed source is always bright, then Method 3 can work best, probably because it avoids the above-mentioned frame-transformation errors.

In conclusion, our approach to the photometry for the microlensing campaign is a variant of MOPEX, a  $\chi^2$  PRF-based minimization modeling of the signal<sup>17</sup>, where we have introduced the freedom to keep some parameters fixed from epoch to epoch, while other parameters are allowed to vary. Specifically, we always keep all other star fluxes fixed, except for those determined to be variables. We usually keep all of the vector angular separations fixed (usually at values determined from a joint fit to the images, but sometimes by direct input from OGLE astrometry). For a few events that remain bright throughout the *Spitzer* observations, we fit for the positions in each frame separately.

In a nutshell, we take advantage of the PRF-fitting procedure and at the same time of the specific features of microlensing and of available data.

### 3. TWO EXAMPLE APPLICATIONS

We illustrate our algorithm with two examples, *Spitzer* targets OGLE-2015-BLG-1395 and OGLE-2015-BLG-0029. These are chosen because they present conditions that are challenging in substantially different ways.

Applications of our algorithm to two other events have already been published: the planetary event OGLE-2015-BLG-0966 (Street et al. 2015) and the binary event with a massive-remnant candidate OGLE-2015-BLG-1285 (Shvartzvald et al. 2015). We note that the case of OGLE-2015-BLG-0966 is particularly interesting because the early light curve yielded satisfactory photometry with Method 1, but not with Method 2. However, later, when the event became brighter, Method 2 became much better (although still not quite as good as Method 1) because it was able to apply its “knowledge” of the microlensed source position from the brighter images to perform precise photometry on the fainter ones.

#### 3.1. OGLE-2015-BLG-1395: High-mag from Earth, Ultrafaint from *Spitzer*

OGLE-2015-BLG-1395 was discovered by the OGLE based on observations with the  $1.4\ \text{deg}^2$  camera on its 1.3 m Warsaw Telescope at the Las Campanas Observatory in Chile using its Early Warning System real-time event-detection software (Udalski et al. 1994; Udalski 2003) on June 19 UT 17:56. The *Spitzer* team contacted OGLE 21 hr later to get an early update on the next night of data and based on this immediately (June 20 UT 14:30) alerted the microlensing community that this was a high-mag event. For results of this monitoring, see A. Cole et al. (2015, in preparation). On June 22, the event met the “objective criteria” for selection according to the protocols of Yee et al. (2015a) and was scheduled for observations at a cadence of 2/day for the first week and 1/day thereafter. The first *Spitzer* observations were three days later, HJD 7199.50, that is, when the ground-based event was 5.3 days past peak and the event had already fallen to  $I = 18.6$ . In fact, when the *Spitzer* data are aligned to the OGLE scale (see below), the first point is at  $I = 19.0$ , corresponding to  $L_{\text{eff}} = 16.2$ , roughly 0.7 mag fainter than the threshold set by Yee et al. (2015a). Hence, it was uncertain whether the parallax of this event could be recovered.

Figure 1 shows four reductions of the *Spitzer* data. MOPEX clearly fails. The reason for this failure is that it “finds” the source at  $\sim 3''\text{--}4''$  from its true position. Regarding the three variants of the new reductions, Method 1 is satisfactory, Method 2 works best, and Method 3 fails completely.

For many years it was believed that satellite parallax measurements required that the satellite observe the event over peak, or at least close enough to peak to determine the satellite-based impact parameter,  $u_{0,\text{sat}}$  (e.g., Gould 1995; Gaudi & Gould 1997). This is because satellite-based parallaxes  $\pi_E$  are basically determined from

$$\pi_E = \frac{\text{AU}}{D_\perp} (\Delta\tau, \Delta\beta); \quad \Delta\tau = \frac{t_{0,\oplus} - t_{0,\text{sat}}}{t_E};$$

$$\Delta\beta = \pm u_{0,\oplus} - \pm u_{0,\text{sat}}, \quad (2)$$

where the subscripts indicate parameters as measured from Earth and the satellite. Here,  $(t_0, u_0, t_E)$  are the standard point-lens microlensing parameters: time of maximum, impact parameter, and Einstein timescale, and  $D_\perp$  is the Earth-satellite separation projected on the sky.

However, Yee et al. (2015a) argued that if the *Spitzer* source flux  $f_s$  could be independently measured (rather than fit from the *Spitzer* light curve as was previously believed necessary), then  $t_{0,\text{sat}}$  and  $u_{0,\text{sat}}$  could be determined even if the *Spitzer* data covered only a fragment of a postpeak light curve by making use of this independent determination of  $f_s$  together with the value of  $t_E$  measured from Earth. From Figure 1 it is clear that OGLE-2015-BLG-1395 provides an excellent way to test this idea.

To implement it, we first derive an estimate of the  $(I_{\text{ogle}} - L_{\text{spitzer}})_s$  color and then incorporate this directly into a joint fit to OGLE+*Spitzer* data. The general method for estimating  $(I - L)_s$  is to measure the source color in some ground-based bands  $X - I$ , then to determine an  $XIL$  ( $X - I$  versus  $I - L$ ) color-color relation based on cross-identified field stars in ground and *Spitzer* images, and finally to apply this relation to the  $(X - L)_s$  color to derive  $(I - L)_s$ . For example, OGLE often has sufficient V-band data during the

<sup>17</sup> In its present version for the fit, we make use of MINUIT (James & Roos 1975) within the CERNLIB package <https://cernlib.web.cern.ch/cernlib/>

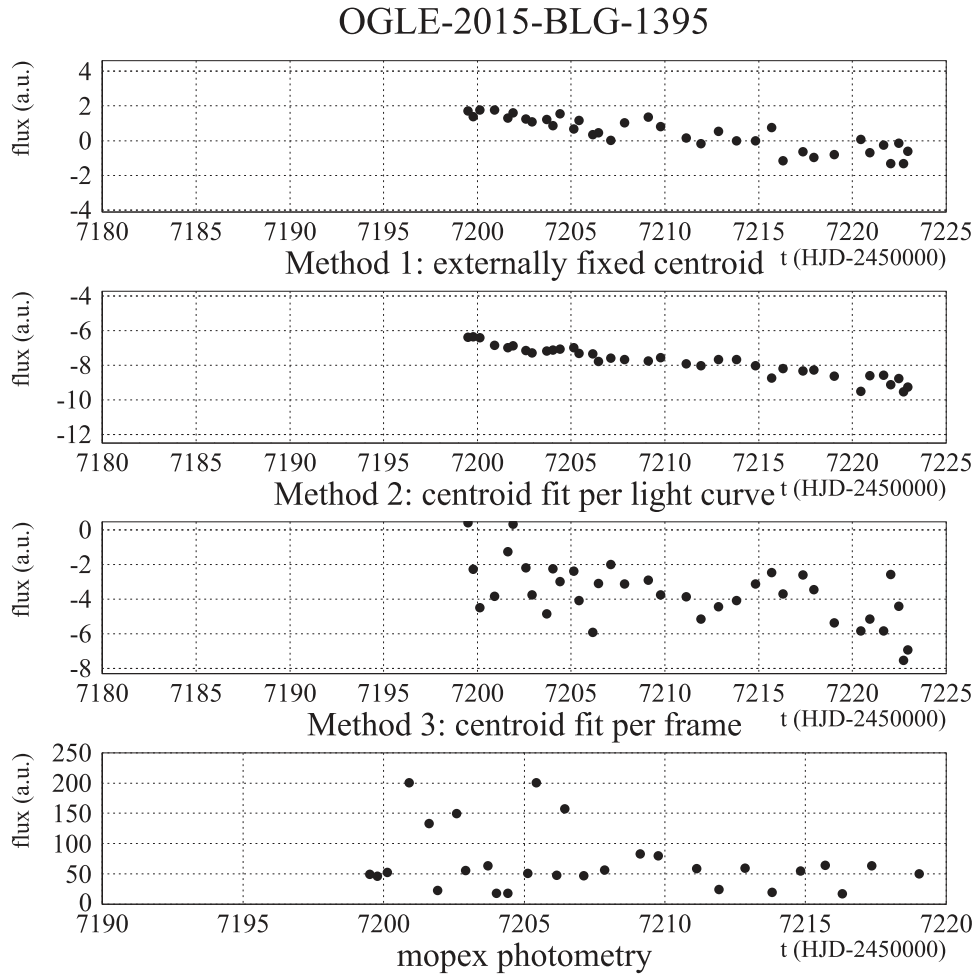


**Figure 1.** *Spitzer* photometry of OGLE-2015-BLG-1395 using four different packages: MOPEX and the three variants of the algorithm presented in this paper; Method 1: externally fixed centroid, Method 2: centroid jointly fitted to entire light curve, Method 3: centroid fitted separately for each epoch. Both MOPEX and Method 3 fail completely and for the same reason: a very faint target.

event to measure  $V - I$  from the ground-based light curve. Alternatively, if the fit to ground-based data shows that the source is unblended, then the baseline ( $V - I$ ) color can be used as the source color. However, in the present case, the event peaked too rapidly to determine  $(V - I)_s$  from the normal cadence of OGLE  $V$ -band data.

We therefore use the simultaneous  $I$  and  $H$  data taken with the dual-channel ANDICAM camera on the 1.3 m SMARTS telescope at CTIO, which acquired substantial data on almost all 2015 *Spitzer* microlensing events, primarily for exactly this purpose. Figure 2 shows a model-independent regression of these data, which yields  $(I - H)_{s, \text{ctio}} = -0.624 \pm 0.007$ . We then form an  $IHL$  color-color diagram (Figure 3). We carry out the color-color regression on stars  $-0.5 < (I - H)_{\text{ctio}} < +0.2$  in order to restrict the sample to warm ( $T > 4300$  K) stars that are in the bulge (and so behind the same column of dust), and we find  $I_{\text{ctio}} - L_{\text{spitzer}} = 1.210(I - H)_{\text{ctio}} - 3.196$  and hence  $(I_{\text{ctio}} - L_{\text{spitzer}})_s = -3.95$ . By regression, we obtain  $I_{\text{ctio}} - I_{\text{ogle}} = 0.73$  and so finally  $(I_{\text{ogle}} - L_{\text{spitzer}})_s = -4.68$ . Here,  $L = 25 - 2.5 \log(F_{\text{spitzer}})$ , where  $F_{\text{spitzer}}$  is the instrumental flux shown in Figure 1 (three upper panels). We estimate an uncertainty of  $\pm 0.1$  on this transformation. We report below on how the final results change with the adopted error bar. In both cases we exclude recursively the outliers, also indicated in the figure, from the regression analysis.

We apply this color constraint to a joint fit to OGLE and *Spitzer* data (Figure 4), wherein the statistical error bars are renormalized so that  $\chi^2/\text{dof} = 1$  for each observatory. This is the standard procedure to account for any possible additional scatter that is due to unmodeled systematics (this issue is further addressed in Section 4). Specifically, the size of the error bars is about 0.08 and 0.12 mag at the bright and the faint end, respectively. Actually, there are four possible fits, parameterized by  $\pm u_{0, \oplus}$  and  $\pm u_{0, \text{sat}}$ , as indicated by Equation (2). From the present standpoint of illustrating how *Spitzer* photometry is carried out and how external constraints are applied to the light curve,  $(t_0, u_0)_{\text{sat}}$  are the primary quantities of interest for these solutions. We find

$$\begin{aligned} (t_0, u_0)_{++} &= (7197.50, +0.280); \\ (t_0, u_0)_{+-} &= (7197.60, +0.282) \end{aligned} \quad (3)$$

$$\begin{aligned} (t_0, u_0)_{--} &= (7197.48, -0.280); \\ (t_0, u_0)_{-+} &= (7197.60, -0.282), \end{aligned} \quad (4)$$

where the first and second subscripts refer to the signs of  $u_0$  for Earth and *Spitzer*, respectively. That is, the naive idea that what is constrained by the *Spitzer* light curve is  $(t_0, |u_0|)_{\text{sat}}$  is confirmed, even though the light curve does not cover the peak. However, this is true only because of the color constraint. If the

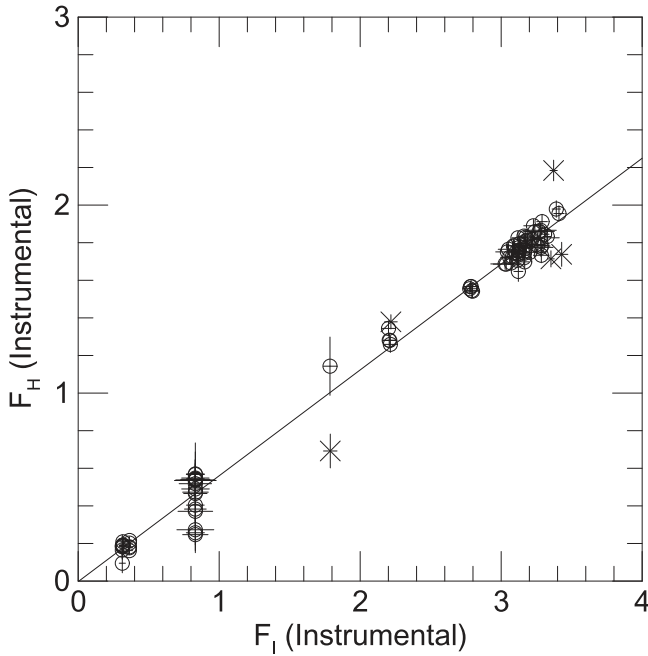


**Figure 2.** Model-independent regression of  $H$ -band on  $I$ -band instrumental fluxes from CTIO-SMARTS observations of OGLE-2015-BLG-1395. These yield a model-independent instrumental source color  $(I - H)_{s, \text{ctio}} = -2.5 \log(F_I/F_H) \approx -2.5 \log(4.00/2.25) = -0.624 \pm 0.007$ . The circles indicate the points used for the color determination, and recursively excluded points are indicated by crosses.

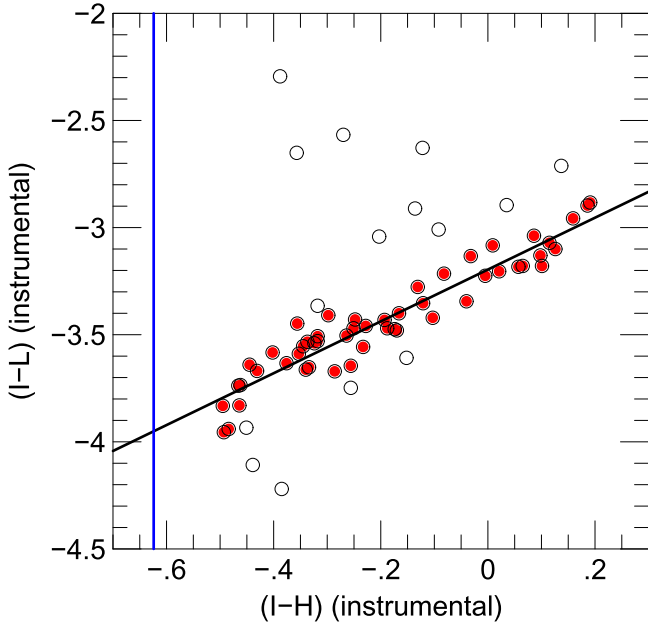


**Figure 3.** Color-color diagram  $I_{\text{ctio}} - L_{\text{spitzer}}$  vs.  $(I - H)_{\text{ctio}}$  based on field stars near OGLE-2015-BLG-1395. Only stars  $-0.5 < (I - H)_{\text{ctio}} < 0.2$  are included in the fit to ensure that it is dominated by bulge stars that are reasonably warm,  $T > 4250$ . The open points have been recursively excluded. The blue line is the source color measured in Figure 2. From this we derive an instrumental color  $(I_{\text{ctio}} - L_{\text{spitzer}})_s = -3.95 \pm 0.10$ .

uncertainty on the color constraint is raised from 0.1 to 0.2, the above results barely change. However, if it is removed, then neither  $t_0$  nor  $u_0$  is meaningfully constrained.

These results confirm the conjecture of Yee et al. (2015a) on the utility of obtaining postpeak light curves from *Spitzer*. In

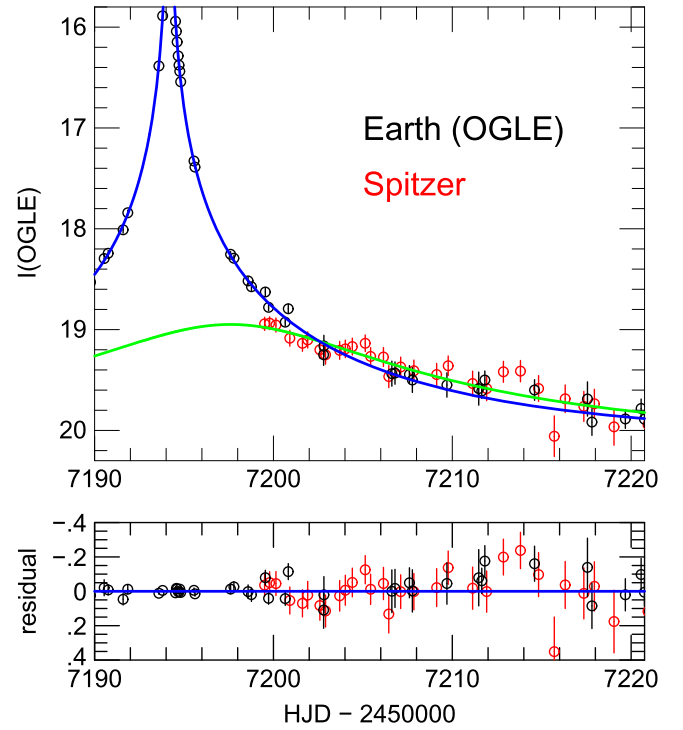


**Figure 4.** Joint point-lens parallax fit of OGLE and *Spitzer* observations of OGLE-2015-BLG-1395, using Method 2 reductions for *Spitzer*. The OGLE data (black) are shown at their observed calibrated  $I$ -band magnitude. The *Spitzer* data (red) are scaled so that their “ $I$  magnitude” corresponds to the same magnification as an OGLE point at this same magnitude. The fit is constrained by the  $(I_{\text{ogle}} - L_{\text{spitzer}})_s = -4.68 \pm 0.10$  source color, which is taken from Figure 3 (after accounting for the instrumental color relation  $I_{\text{ctio}} - I_{\text{ogle}} = 0.68$ ).

particular, they imply that planet-sensitive high-magnification events should be “subjectively selected,” even when it is clear that *Spitzer* observations cannot begin until several days after peak.

### 3.2. OGLE-2015-BLG-0029: Bright Source in a Crowded Field

OGLE-2015-BLG-0029 was discovered by OGLE on 2015 February 12. On May 10 it was “subjectively selected” for *Spitzer* observations with an “objective” 1/day cadence. This was long before *Spitzer* observations began, which is critical for establishing the planet sensitivity of events that do not meet objective criteria. According to the protocols of Yee et al. (2015a), planets and planet sensitivity for subjectively selected events begin with the time of selection, not the start of *Spitzer* observations. As it turned out, on June 1, the event met the objective criteria for rising events as laid out in Yee et al. (2015a). Since the cadence for *Spitzer* observations of objectively selected events was the same as that specified on May 10, *Spitzer* observations of OGLE-2015-BLG-0029 were scheduled objectively. These observations began on June 11, when the event first became visible by *Spitzer*, and continued until the end of the campaign on July 19. As specified in Yee et al. (2015a), a cadence of “1/day” determines the relative frequency with which an event should be observed, and the actual cadence is set by this and the available time. Hence, this event received extra observations at the beginning and end of the campaigns as competing events were eliminated because of *Spitzer*’s Sun-exclusion angle. Altogether, it was observed at 52 epochs.

In contrast to OGLE-2015-BLG-1395, OGLE-2015-BLG-0029 is a very bright event with  $I \sim 14.5$ –15. However, similar

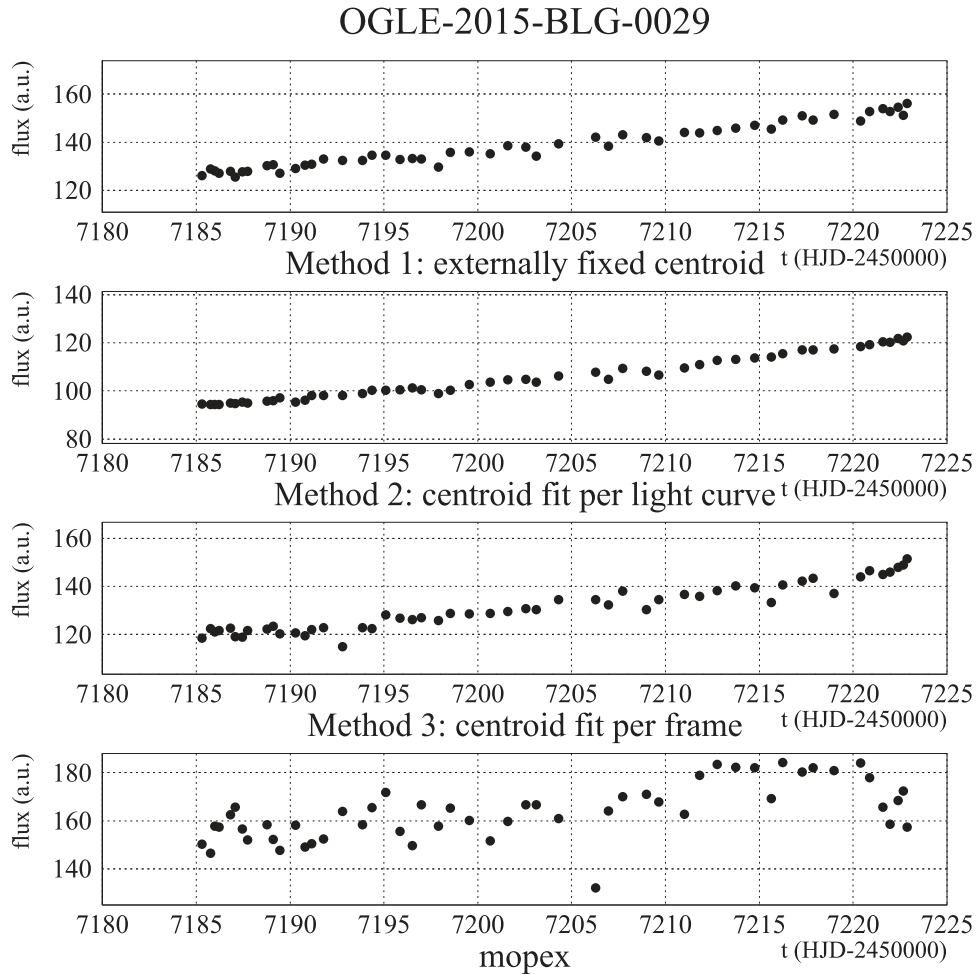


**Figure 5.** Four reductions of OGLE-2015-BLG-0029 *Spitzer* data. From top to bottom they are Methods 1, 2, 3, and the standard MOPEX pipeline. Although the microlensed source is bright, it is blended with a  $\sim 5$  times fainter star at  $1''$ , which is similar to the first Airy null ( $1''.06$ ) but smaller than an IRAC pixel ( $1''.2$ ). Method 2 copes with this situation best. MOPEX becomes completely confused if it is “informed” of the existence of this blend (not shown) and does better if it treats the blend as coincident with the microlensed source (displayed), but the results are still quite poor when compared to Method 2.

to OGLE-2015-BLG-1395, the MOPEX pipeline basically fails to measure the light curve for this event, albeit not catastrophically, as was the case for OGLE-2015-BLG-1395. See Figure 5. The reason that MOPEX fails is crowding, in particular the presence of an  $I = 17$  neighbor at  $0''.97$ . This neighbor, which is  $\sim 5$  times fainter than the microlensed source at  $3.6 \mu\text{m}$  at its faintest (first) *Spitzer* epoch, is clearly resolved in OGLE data but unresolved in individual IRAC images. What makes this case especially instructive is that the source lies almost exactly at the first Airy null ( $1''.06$ ), so it is resolvable in principle, but within one IRAC pixel ( $1''.2$ ). If MOPEX is “informed” about the presence of this source, then it assigns the source wildly varying positions and fluxes, which impacts the microlensing light curve catastrophically. If MOPEX is not “informed” (and so treats the microlensed source and the nearby blend as having a common position), it does better but still has more than an order of magnitude greater scatter than our new algorithm, particularly in its Method 2 variant.

#### 4. DESCRIPTION OF CATALOG

In Table 1 we list the 170 events monitored in 2015. For each, we report the event name, the coordinates, the first and

last day of observation, and the number of observed epochs. The events were chosen based on the microlensing alerts provided by the OGLE (Udalski et al. 2015a) and MOA (Bond et al. 2004) collaborations. The current analysis is based on the preliminary reduced data made available by the *Spitzer* Science Center almost in real time (on average, 2–3 days after the observations). The final reduction of the data is now publicly available at the NASA/IPAC Infrared Science Database (IRSA, <http://irsa.ipac.caltech.edu/frontpage/>). Besides the full table, in the online material we provide the light curves for the full sample of observed events, similar to Figures 1 and 5 (excluding the MOPEX reductions). As an example we show (Figure 6) the light curve for the planetary event OGLE-2015-BLG-0966 (Street et al. 2015). Finally, an updated version of our photometry solutions is kept at a publicly available website.<sup>18</sup> In particular, we provide tables with the data for all three reductions discussed in the text. The flux is expressed in arbitrary units. In some cases, none of the reductions look satisfactory, which may just reflect that the absolute level of source flux variations is very low. The reported error is the purely statistical error from the fitting procedure based on the IRAC uncertainty images (and so underestimates the true

<sup>18</sup> <http://www.astronomy.ohio-state.edu/Spitzer2015/>



## OGLE-2015-BLG-0966

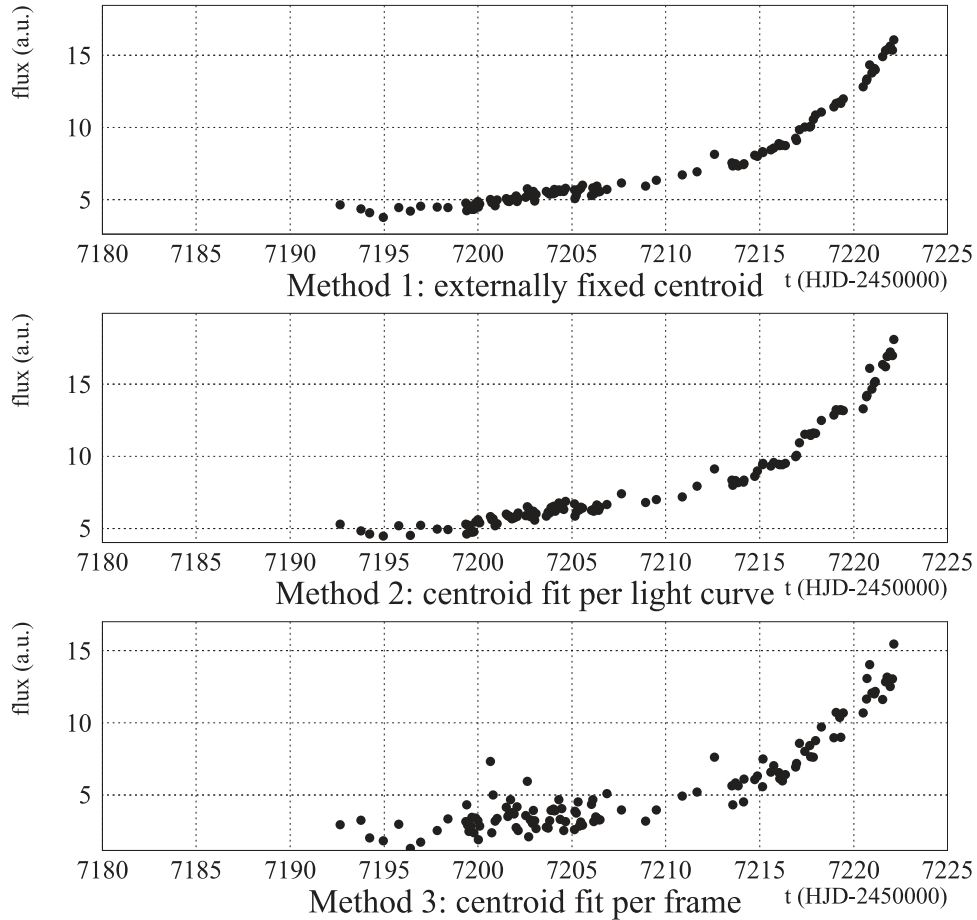


**Figure 6.** Three reductions of the *Spitzer* data. From top to bottom they are Methods 1, 2, and 3. The remaining 169 sources are available as a figure set in the electronic edition.

(The complete figure set (170 images) is available.)

uncertainties). In particular, we attribute any additional scatter to systematics due to unmodeled physics (a completely generic feature for all photometry algorithms in crowded fields). These must be considered case by case during the modeling of the events. We note that a single parameter (the “background”) must account for the combined effects of unresolved stars and incompletely modeled wings of distant bright stars, in addition to the true background. It is therefore expected that faint stars will sometimes take on negative flux values. This has no impact on microlensing analyses, which fit only the flux variations and similarly absorb the constant-flux term into a nuisance parameter “ $f_b$ .”

We emphasize that for events of special scientific interest, further work on reductions may improve the light curve. In particular, for events in which the external knowledge of the source position is important, such as OGLE-2015-BLG-1395, this can often be improved by measuring this position from OGLE difference images. An additional key aspect of the analysis that may be improved on a case-by-case basis is the choice of blend stars to be fitted simultaneously with the microlensed source. An additional aspect that may become critical, which is not taken into account in the standard pipeline and which requires further specific analyses, is saturation and nonlinearities in the response of the detector when approaching the pixel full well. An example is that of the *Spitzer* light curve

for the microlensing event OGLE-2015-BLG-0763, which is presented in the online catalog without the special treatment required to deal with saturation. Because this event is of special interest, it was reanalyzed making use of specific procedures to deal with saturation and nonlinearity (Zhu et al. 2015a).

## 5. DISCUSSION

The principal characteristics of the data set that drove the design of the algorithms described here will also be present in the *Kepler* K2 (Howell et al. 2014) microlensing data. These include

1. undersampled PSF,
2. nonuniform pixel response,
3. many stars overlapping the microlensed source,
4. most (or all) of the other stars nonvariable,
5. external astrometric catalog at higher resolution,
6. dithered exposures, and
7. many epochs.

Hence, it may be profitable to employ similar algorithms on the K2 data set. While the first microlensing data will not be available at least until 2016 June, there are already K2 test data from other crowded fields on which these algorithms could be developed.



**Table 1**  
Observed Events

Event	R.A. (J2000)	Decl. (J2000)	<i>Spitzer</i>		
			First	Last	Epochs
	(degrees)	(degrees)	(HJD)	(HJD)	
MOA-BLG-2015-020	268.219917	−32.485861	7183.95	7221.76	61
MOA-BLG-2015-079	268.085334	−31.295665	7183.66	7221.76	112
MOA-BLG-2015-117	268.792652	−35.080247	7184.10	7212.60	45
MOA-BLG-2015-220	271.832485	−25.467555	7187.12	7222.96	48
MOA-BLG-2015-237	269.467804	−31.472354	7184.97	7223.06	54
MOA-BLG-2015-240	270.585946	−31.996441	7185.80	7212.75	37
MOA-BLG-2015-245	269.321669	−27.857411	7184.99	7222.60	78
MOA-BLG-2015-267	269.214339	−30.775359	7199.49	7222.65	39
MOA-BLG-2015-282	272.572708	−29.265556	7199.71	7222.94	29
MOA-BLG-2015-287	270.125760	−33.017623	7199.35	7222.89	36
OGLE-BLG-2014-0298	268.565625	−31.018083	7185.73	7221.84	25
OGLE-BLG-2014-0613	268.490300	−28.572670	7183.98	7221.81	158
OGLE-BLG-2015-0011	269.217833	−29.283250	7184.96	7222.59	53
OGLE-BLG-2015-0022	268.090792	−29.785028	7183.67	7221.05	60
OGLE-BLG-2015-0029	269.944167	−28.644944	7185.31	7222.89	52
OGLE-BLG-2015-0034	270.580333	−27.516083	7186.01	7222.92	62
OGLE-BLG-2015-0060	269.993125	−27.780944	7185.78	7222.90	50
OGLE-BLG-2015-0081	268.653000	−28.996278	7184.10	7221.82	57
OGLE-BLG-2015-0145	270.177833	−35.154056	7185.29	7222.88	51
OGLE-BLG-2015-0149	270.288208	−32.557694	7185.80	7222.93	49
OGLE-BLG-2015-0195	266.790792	−33.417278	7182.39	7220.58	70
OGLE-BLG-2015-0196	266.492958	−32.956778	7182.39	7220.56	70
OGLE-BLG-2015-0211	262.359083	−30.981750	7180.20	7216.80	109
OGLE-BLG-2015-0238	265.708250	−36.818500	7182.37	7219.17	75
OGLE-BLG-2015-0244	268.240625	−28.980889	7183.97	7221.75	59
OGLE-BLG-2015-0254	271.553292	−26.850194	7186.87	7222.96	49
OGLE-BLG-2015-0326	274.074625	−26.338139	7199.73	7223.03	29
OGLE-BLG-2015-0350	268.248583	−31.820278	7183.95	7221.76	61
OGLE-BLG-2015-0379	269.104292	−29.574056	7184.61	7222.58	54
OGLE-BLG-2015-0388	268.468917	−28.534028	7183.98	7221.81	66
OGLE-BLG-2015-0401	264.081167	−27.774139	7180.19	7213.03	94
OGLE-BLG-2015-0444	262.917375	−30.673111	7180.20	7216.79	84
OGLE-BLG-2015-0448	272.559917	−31.752611	7187.54	7223.04	211
OGLE-BLG-2015-0461	270.043208	−28.156944	7185.79	7222.90	58
OGLE-BLG-2015-0477	273.200500	−25.014028	7188.88	7222.97	45
OGLE-BLG-2015-0479	265.918958	−35.509278	7182.38	7219.17	67
OGLE-BLG-2015-0529	270.264667	−29.922917	7185.79	7222.92	51
OGLE-BLG-2015-0561	267.224542	−29.674444	7183.09	7220.61	68
OGLE-BLG-2015-0565	269.153708	−29.128056	7184.62	7222.59	53
OGLE-BLG-2015-0572	272.847750	−25.473861	7188.88	7222.97	44
OGLE-BLG-2015-0607	274.049625	−27.451306	7189.13	7223.03	54
OGLE-BLG-2015-0642	263.539458	−24.882528	7192.99	7216.78	25
OGLE-BLG-2015-0692	268.079708	−28.133917	7185.70	7221.07	73
OGLE-BLG-2015-0703	269.048583	−29.853389	7184.47	7222.17	65
OGLE-BLG-2015-0709	266.113292	−34.442972	7182.38	7219.16	74
OGLE-BLG-2015-0713	272.660042	−28.412083	7213.65	7223.01	28
OGLE-BLG-2015-0749	264.955708	−27.511722	7180.78	7206.48	59
OGLE-BLG-2015-0761	272.084667	−25.443056	7187.52	7222.97	46
OGLE-BLG-2015-0763	263.097542	−29.302694	7180.19	7216.78	142
OGLE-BLG-2015-0769	265.670083	−27.368833	7182.40	7219.15	59
OGLE-BLG-2015-0772	269.421583	−28.143139	7184.99	7222.60	54
OGLE-BLG-2015-0798	271.680583	−27.590167	7186.86	7222.95	47
OGLE-BLG-2015-0802	266.514625	−36.497917	7182.38	7220.57	76
OGLE-BLG-2015-0808	267.184833	−33.102278	7199.31	7220.59	25
OGLE-BLG-2015-0828	267.132917	−34.184778	7183.08	7220.58	72
OGLE-BLG-2015-0843	271.197042	−27.176472	7186.87	7222.95	61
OGLE-BLG-2015-0845	271.088708	−31.580556	7186.24	7222.93	148
OGLE-BLG-2015-0877	273.676958	−27.970917	7188.92	7212.92	29
OGLE-BLG-2015-0912	265.957583	−26.519944	7182.41	7219.15	57
OGLE-BLG-2015-0914	269.311750	−29.760139	7184.96	7222.58	53
OGLE-BLG-2015-0925	270.259292	−26.384889	7199.67	7222.91	29
OGLE-BLG-2015-0926	270.883792	−26.135806	7199.67	7222.91	29

**Table 1**  
(Continued)

Event	R.A. (J2000)	Decl. (J2000)	<i>Spitzer</i>		
			First	Last	Epochs
	(degrees)	(degrees)	(HJD)	(HJD)	
OGLE-BLG-2015-0930	264.393917	-25.512667	7180.21	7218.07	111
OGLE-BLG-2015-0941	272.348083	-25.762056	7187.53	7222.98	47
OGLE-BLG-2015-0944	265.258000	-27.853806	7181.09	7198.12	42
OGLE-BLG-2015-0955	273.709833	-27.006833	7213.88	7223.01	14
OGLE-BLG-2015-0958	267.754958	-28.416861	7183.32	7221.06	64
OGLE-BLG-2015-0961	268.146375	-30.080361	7185.69	7221.75	131
OGLE-BLG-2015-0965	269.291083	-28.961056	7184.99	7222.59	52
OGLE-BLG-2015-0966	268.754250	-29.047111	7192.64	7222.14	119
OGLE-BLG-2015-0968	268.985833	-28.854083	7184.47	7222.19	56
OGLE-BLG-2015-0977	272.061375	-26.159472	7187.53	7222.96	47
OGLE-BLG-2015-0984	263.875167	-26.553778	7185.84	7217.51	39
OGLE-BLG-2015-0987	268.193708	-28.361222	7183.97	7221.07	65
OGLE-BLG-2015-1020	263.050417	-29.781722	7180.19	7216.78	108
OGLE-BLG-2015-1076	270.744792	-32.853694	7192.81	7222.94	135
OGLE-BLG-2015-1077	274.478083	-22.992611	7192.93	7223.03	64
OGLE-BLG-2015-1084	271.146417	-26.168028	7186.87	7212.80	35
OGLE-BLG-2015-1095	267.693875	-32.708167	7183.24	7221.04	65
OGLE-BLG-2015-1096	267.872333	-32.153694	7183.40	7221.04	62
OGLE-BLG-2015-1100	263.669042	-29.885194	7180.20	7217.52	84
OGLE-BLG-2015-1109	270.213083	-30.645139	7185.80	7191.80	13
OGLE-BLG-2015-1112	273.535250	-25.482778	7188.79	7222.98	51
OGLE-BLG-2015-1113	264.277208	-27.299083	7180.18	7218.10	88
OGLE-BLG-2015-1123	273.648042	-26.507389	7188.88	7223.01	70
OGLE-BLG-2015-1124	273.253750	-27.532861	7188.89	7206.39	23
OGLE-BLG-2015-1129	266.413125	-27.160028	7182.41	7185.33	18
OGLE-BLG-2015-1136	268.557583	-28.708361	7185.71	7198.40	24
OGLE-BLG-2015-1145	269.451042	-29.080444	7185.63	7222.84	79
OGLE-BLG-2015-1148	270.259625	-28.686111	7185.79	7198.57	22
OGLE-BLG-2015-1150	273.049208	-25.661694	7199.72	7223.05	121
OGLE-BLG-2015-1153	264.317792	-29.426389	7193.01	7218.08	50
OGLE-BLG-2015-1161	267.618375	-29.979222	7192.59	7220.61	34
OGLE-BLG-2015-1167	269.024500	-28.626361	7184.46	7222.20	56
OGLE-BLG-2015-1172	268.545417	-31.103194	7185.73	7198.41	24
OGLE-BLG-2015-1184	268.514458	-30.311250	7183.96	7185.41	10
OGLE-BLG-2015-1187	268.657792	-31.681222	7199.45	7222.16	27
OGLE-BLG-2015-1188	268.877125	-31.281667	7184.34	7222.17	56
OGLE-BLG-2015-1189	270.735000	-30.373056	7192.80	7222.93	87
OGLE-BLG-2015-1194	261.049625	-28.947472	7207.44	7215.02	9
OGLE-BLG-2015-1196	266.466667	-24.287278	7182.41	7198.06	37
OGLE-BLG-2015-1197	264.229917	-29.782028	7207.42	7218.09	31
OGLE-BLG-2015-1204	268.927083	-29.384306	7199.50	7222.18	27
OGLE-BLG-2015-1207	267.709667	-23.445500	7192.93	7220.56	31
OGLE-BLG-2015-1212	268.103292	-29.181111	7185.70	7206.09	92
OGLE-BLG-2015-1221	268.418792	-32.279306	7199.33	7221.94	101
OGLE-BLG-2015-1223	265.690333	-27.528333	7182.40	7212.95	53
OGLE-BLG-2015-1227	268.327417	-29.652833	7199.41	7221.83	26
OGLE-BLG-2015-1232	267.641125	-32.739639	7185.66	7191.98	16
OGLE-BLG-2015-1234	267.179917	-24.520028	7192.93	7220.56	31
OGLE-BLG-2015-1236	265.421375	-27.809278	7185.81	7219.15	42
OGLE-BLG-2015-1241 <sup>a</sup>	269.529708	-27.932000	7185.63	7198.49	35
OGLE-BLG-2015-1256	269.537083	-28.769083	7185.77	7206.27	31
OGLE-BLG-2015-1262	267.523792	-30.712611	7185.68	7206.04	33
OGLE-BLG-2015-1263	267.717208	-32.380389	7185.67	7206.03	32
OGLE-BLG-2015-1264	264.976250	-34.584722	7192.51	7219.17	31
OGLE-BLG-2015-1268	269.207375	-21.899333	7192.61	7212.93	48
OGLE-BLG-2015-1281	273.034625	-27.167694	7192.86	7222.95	36
OGLE-BLG-2015-1285	264.846875	-27.820278	7199.81	7218.09	39
OGLE-BLG-2015-1288	267.516625	-33.368472	7192.52	7221.03	35
OGLE-BLG-2015-1289	269.461583	-28.217306	7206.94	7222.83	22
OGLE-BLG-2015-1295	270.226042	-27.302139	7199.39	7223.08	127
OGLE-BLG-2015-1297	268.087542	-29.683806	7192.59	7206.05	17
OGLE-BLG-2015-1303	273.970333	-30.373194	7199.42	7223.02	68

**Table 1**  
(Continued)

Event	R.A. (J2000)	Decl. (J2000)	<i>Spitzer</i>		
			First	Last	Epochs
	(degrees)	(degrees)	(HJD)	(HJD)	
OGLE-BLG-2015-1309	264.693250	-27.479472	7199.82	7218.10	20
OGLE-BLG-2015-1315	266.672583	-33.458194	7206.71	7220.57	17
OGLE-BLG-2015-1319	269.443333	-32.472194	7206.95	7223.07	22
OGLE-BLG-2015-1325	266.423625	-35.957278	7213.41	7220.83	18
OGLE-BLG-2015-1328	267.063208	-32.687778	7199.32	7206.02	8
OGLE-BLG-2015-1339	263.321917	-30.271222	7199.91	7217.52	18
OGLE-BLG-2015-1341	268.563667	-28.350167	7199.47	7221.81	25
OGLE-BLG-2015-1344	268.934542	-27.940028	7192.67	7222.32	57
OGLE-BLG-2015-1346	269.806958	-28.936611	7192.79	7222.88	37
OGLE-BLG-2015-1348	269.487708	-30.509417	7199.55	7223.06	29
OGLE-BLG-2015-1350	266.685583	-36.592889	7199.29	7220.57	73
OGLE-BLG-2015-1352	265.141875	-27.338306	7207.37	7218.08	13
OGLE-BLG-2015-1366	268.289250	-21.944056	7213.90	7221.74	10
OGLE-BLG-2015-1368	267.945083	-29.575167	7199.34	7221.06	77
OGLE-BLG-2015-1370	268.956667	-29.124111	7206.90	7222.18	19
OGLE-BLG-2015-1371	268.665875	-29.093944	7206.87	7221.83	18
OGLE-BLG-2015-1374	271.134375	-26.887806	7213.64	7223.00	28
OGLE-BLG-2015-1378	264.834792	-22.976222	7199.79	7218.06	20
OGLE-BLG-2015-1383	268.651292	-28.702250	7213.53	7221.94	22
OGLE-BLG-2015-1392	264.095125	-27.298917	7213.68	7217.82	11
OGLE-BLG-2015-1395	271.783917	-26.303333	7199.51	7222.96	36
OGLE-BLG-2015-1400	268.109625	-28.866250	7213.47	7221.55	20
OGLE-BLG-2015-1403	267.882875	-29.340361	7206.79	7221.06	17
OGLE-BLG-2015-1412	270.124875	-27.435361	7207.00	7223.05	35
OGLE-BLG-2015-1416	270.937500	-26.848056	7207.07	7222.92	21
OGLE-BLG-2015-1420	271.477500	-28.557361	7213.65	7223.02	28
OGLE-BLG-2015-1424	264.063292	-29.642833	7199.83	7218.09	20
OGLE-BLG-2015-1425	263.142958	-30.716333	7213.69	7217.10	9
OGLE-BLG-2015-1435	269.842167	-27.219222	7199.57	7206.27	8
OGLE-BLG-2015-1440	270.973167	-27.707417	7213.64	7222.99	28
OGLE-BLG-2015-1447	269.233417	-31.941111	7213.50	7222.81	27
OGLE-BLG-2015-1448	270.939333	-27.852194	7207.04	7222.99	35
OGLE-BLG-2015-1450	270.210000	-28.671028	7213.51	7223.07	56
OGLE-BLG-2015-1457	267.857167	-30.436389	7206.78	7221.05	17
OGLE-BLG-2015-1467	265.107500	-23.801389	7207.38	7212.97	7
OGLE-BLG-2015-1469	265.266583	-24.848944	7213.67	7218.92	13
OGLE-BLG-2015-1470	268.501833	-31.592806	7206.82	7221.84	18
OGLE-BLG-2015-1481	268.008083	-30.985028	7213.48	7221.54	20
OGLE-BLG-2015-1482	267.630542	-30.888694	7206.73	7221.04	17
OGLE-BLG-2015-1485	265.380250	-24.214972	7207.35	7218.92	20
OGLE-BLG-2015-1492	268.686000	-29.707361	7213.48	7221.96	22
OGLE-BLG-2015-1500	272.021583	-27.445611	7207.12	7212.84	7
OGLE-BLG-2015-1521	267.485792	-21.411889	7213.66	7220.82	17
OGLE-BLG-2015-1530	269.018958	-28.240472	7213.53	7222.38	24
OGLE-BLG-2015-1533	269.048083	-29.476417	7213.51	7222.39	24
OGLE-BLG-2015-1553	265.857042	-23.377750	7213.67	7219.14	14

**Notes.** We report name, target coordinates, and information about *Spitzer* observations for the 170 microlensing events monitored during the 2015 *Spitzer* microlensing campaign. We note that two out of the 10 MOA events have also been observed by the OGLE collaboration (specifically, MOA-BLG-2015-020 and MOA-BLG-2015-245 are also known as OGLE-BLG-2015-0102 and OGLE-BLG-2015-1286, respectively), and 64 out of the 160 OGLE events have also been observed by the MOA collaboration (for the details on this we refer to the MOA microlensing alert web page [http://www.phys.canterbury.ac.nz/moa/microlensing\\_alerts.html](http://www.phys.canterbury.ac.nz/moa/microlensing_alerts.html)). In Figure 6 we show the corresponding light curves for the three variants of our photometry reduction for all of the events (online material). The first method, which relies on an analysis based on the OGLE online catalog of nearby stars to the microlensed source, is not presented for MOA-only events and for four OGLE events (OGLE-BLG-2015-0561, OGLE-BLG-2015-0941, OGLE-BLG-2015-1112, and OGLE-BLG-2015-1234).

<sup>a</sup> This event is also known as OGLE-BLG-2015-1253.

All of the above characteristics, with the exception of (5) and the partial exception of (3), apply to *WFIRST* (Spergel et al. 2013a, 2013b) as well. In some respects, the challenges of *WFIRST* may seem less pressing. However, if having available

a source catalog at higher resolution proves important for *WFIRST* (as it so far appears to be for *Spitzer*), then now is the time to remedy its absence, before the demise of the *Hubble Space Telescope*.

We thank J. Ingalls for a useful discussion about PRF fitting with IRAC data. Work by S.C.N., A.G., S.C., J.C.Y., and W.Z. was supported by JPL grant 1500811. Work by Y.S. was supported by an appointment to the NASA Postdoctoral Program at the Jet Propulsion Laboratory, administered by Oak Ridge Associated Universities through a contract with NASA. Work by J.C.Y. was performed under contract with the California Institute of Technology (Caltech)/Jet Propulsion Laboratory (JPL) funded by NASA through the Sagan Fellowship Program executed by the NASA Exoplanet Science Institute. This work is based (in part) on observations made with the *Spitzer Space Telescope*, which is operated by the Jet Propulsion Laboratory, California Institute of Technology, under a contract with NASA. Support for this work was provided by NASA through an award issued by JPL/Caltech.

The OGLE project has received funding from the National Science Centre, Poland, grant MAESTRO 2014/14/A/ST9/00121 to AU.

## REFERENCES

- Alard, C., & Lupton, R. H. 1998, *ApJ*, **503**, 325
- Anderson, J., & King, I. R. 2000, *PASP*, **112**, 1360
- Bond, I. A., Udalski, A., Jorzyński, M., et al. 2004, *ApJ*, **606**, 155
- Calchi Novati, S., Gould, A., Udalski, A., et al. 2015, *ApJ*, **804**, 20
- Charbonneau, D., Allen, L. E., Megeath, S. T., et al. 2005, *ApJ*, **626**, 523
- Deming, D., Seager, S., Richardson, L. J., & Harrington, J. 2005, *Natur*, **434**, 740
- Dong, S., Udalski, A., Gould, A., et al. 2007, *ApJ*, **664**, 862
- Fazio, G. G., Ashby, M. L. N., Barnby, P., et al. 2004, *ApJS*, **154**, 39
- Gaudi, B. S., & Gould, A. 1997, *ApJ*, **477**, 152
- Gould, A. 1995, *ApJL*, **441**, L21
- Gould, A. 1999, *ApJ*, **514**, 869
- Gould, A., Dong, S., Gaudi, B. S., et al. 2010, *ApJ*, **720**, 1073
- Gould, A., & Horne, K. 2013, *ApJ*, **779**, 28
- Griest, K., & Safizadeh, N. 1998, *ApJ*, **500**, 37
- Howell, S. B., Sobek, C., Haas, M., et al. 2014, *PASP*, **126**, 398
- Ingalls, J., Krick, J., Carey, S., et al. 2012, *Proc. SPIE*, **8442**, 1Y
- James, F., & Roos, M. 1975, *CoPhC*, **10**, 343
- Lauer, T. R. 1999, *PASP*, **111**, 1434
- Makovoz, D., & Marleau, F. R. 2005, *PASP*, **117**, 1113
- Refsdal, S. 1966, *MNRAS*, **134**, 315
- Schechter, P. L., Mateo, M., & Saha, A. 1993, *PASP*, **105**, 1342
- Shvartzvald, Y., Udalski, A., Gould, A., et al. 2015, *ApJ*, in press (arXiv:1508.06636)
- Spergel, D., Gehrels, N., Breckinridge, J., et al. 2013a, arXiv:1305.5422
- Spergel, D., Gehrels, N., Breckinridge, J., et al. 2013b, arXiv:1305.5425
- Storrie-Lombardi, L. J., & Dodd, S. R. 2010, *Proc. SPIE*, **7737**, 0L
- Street, R., Udalski, A., Calchi Novati, S., et al. 2015, *ApJ*, submitted (arXiv:1508.07027)
- Udalski, A. 2003, *AcA*, **53**, 291
- Udalski, A., Szymanski, M., Kaluzny, J., et al. 1994, *AcA*, **44**, 317
- Udalski, A., Szymański, M. K., & Szymański, G. 2015a, *AcA*, **65**, 1
- Udalski, A., Yee, J. C., Gould, A., et al. 2015b, *ApJ*, **799**, 237
- Yee, J. C., Gould, A., Beichman, C., et al. 2015a, *ApJ*, **810**, 155
- Yee, J. C., Udalski, A., Calchi Novati, S., et al. 2015b, *ApJ*, **802**, 76
- Zhu, W., Calchi Novati, S. A., Gould, A., et al. 2015a, *ApJ*, submitted (arXiv:1510.02097)
- Zhu, W., Udalski, A., Gould, A., et al. 2015b, *ApJ*, **805**, 8